Atomic layer deposition of vanadium oxide to reduce parasitic absorption and improve stability in n-i-p perovskite solar cells for tandems

James A. Raiford[1†], Rebecca A. Belisle[2,3†], Kevin A. Bush[3], Rohit Prasanna[3,4], Axel F. Palmstrom[4], Michael D. McGehee[5], Stacey F. Bent*[1]

[1] Department of Chemical Engineering, Stanford University, Stanford, CA 94305, USA
[2] Physics Department, Wellesley College, Wellesley, MA 02481, USA
[3] Department of Materials Science and Engineering, Stanford University, Stanford, CA 94305, USA
[4] National Renewable Energy Laboratory, Golden, Colorado 80401, USA
[5] Department of Chemical and Biological Engineering, University of Colorado, Boulder, CO 80309, USA

[†]These authors contributed equally to this work.
*Corresponding author: sbent@stanford.edu

Abstract

Two critical issues associated with semi-transparent, n-i-p perovskite solar cells for 2-terminal tandem devices are parasitic absorption and long-term instability associated with the widely used spiro-OMeTAD and MoO_x hole transport and buffer layers, respectively. In this work, we present an alternative hole contact bilayer that consists of a 30 nm undoped layer of spiro-TTB in conjunction with 9 nm of air-stable vanadium oxide (VO_x) deposited via atomic layer deposition. The low absorption of UV and visible light in this bilayer results in the fabrication of a semi-transparent perovskite cell with 18.9 mA/cm^2 of photocurrent, a 14% increase compared to the 16.6 mA/cm^2 generated in a control device with 150 nm of doped spiro-OMeTAD. The ALD VO_x buffer layer shows promise as a stable alternative to MoO_x; an unencapsulated $Cs_{0.17}FA_{0.83}Pb(Br_{0.17}I_{0.83})_3$ device with ALD VO_x/ITO as the top contact maintains its efficiency following 1000 hours at 85°C in a N_2 environment. Lastly, we use transfer matrix modeling of the optimized perovskite stack to predict its optical performance in a monolithic tandem cell with heterojunction silicon.

Introduction

Multi-junction solar cells are a proven pathway towards surpassing the power conversion efficiency (PCE) limits of single-junction devices. In particular, tandem cells that utilize crystalline silicon (c-Si) technology as the low band gap semiconductor are particularly attractive due to the high efficiency and well-established, low-cost manufacturing of c-Si modules.[1] Over the past several years, lead-halide perovskite solar cells (PSCs) have demonstrated a meteoric rise in efficiency to over 23% PCE for single junction devices.[2–6] This rapid improvement in performance, along with other favorable properties such as a tunable band gap[7,8] and strong optical absorption[9] makes PSCs a suitable candidate for the wide band gap cell of high-performance, low-cost tandems.[10–15]

To date, the highest published efficiencies for 2-terminal PSC/c-Si tandems in the n-i-p and p-i-n architectures are 22.5% and 25.4% PCE, respectively.[15,16] Not only is the performance of the n-i-p tandem worse than that of its p-i-n counterpart, it also falls below 23.7% PCE – the current record efficiency for a single-junction PSC in the same architecture.[6] The primary reason for this discrepancy is a lower photocurrent in n-i-p tandems due to parasitic light absorption and reflection associated with the PSC hole transport layers (HTLs).[17,18] Another important contributor is losses incurred by replacing an opaque contact with a transmissive one. While a sputtered transparent conducting oxide (TCO) is an effective front contact for semi-transparent PSCs and improves thermal stability of devices by acting as a diffusion barrier,[19,20] it requires an additional buffer layer to protect the underlying solar cell from damage due to high kinetic energy particles during sputtering.[21,22] Recently, SnO_2 deposited by atomic layer deposition (ALD) as a sputter buffer layer has been instrumental in the fabrication of stable and highly efficient 2-terminal p-i-n PSC/c-Si tandems.[12,16,23] Its most common counterpart for n-i-p tandems is molybdenum oxide (MoO_x), typically around 10 nm thick, deposited by thermal evaporation.[15,24]

While the MoO_x layer effectively prevents the solar cell from sputter damage, it has been shown to react with the perovskite, which negatively impacts device efficiency and stability.[25–27] Further studies have demonstrated that this degradation can be reduced in single-junction cells with an organic interlayer and an aluminum electrode, in part by the formation of aluminum oxide at the

MoO_x/Al interface.[28] However, the long-term stability of semi-transparent devices with MoO_x has yet to be tested, and preliminary results on MoO_x reactivity and the impacts of increasing MoO_x thickness on stability are not encouraging.[25–27] One potential substitute for MoO_x as a buffer layer in semi-transparent PSCs is vanadium oxide (VO_x). VO_x is a wide bandgap semiconductor (> 2 eV) with a low-lying conduction band.[29] Unlike most common HTLs, such as NiO_x (which transports holes through its valence band), VO_x has a multitude of defect states formed by oxygen vacancies that allow for charge transport within the band gap below the metal oxide's conduction band.[30]

VO_x has been previously reported as an HTL in p-i-n PSCs, either by itself[31–33] or as part of a bilayer.[32–36] In these devices, the VO_x is solution-processed on a substrate prior to deposition of the perovskite layer. These solution-based deposition methods are less attractive for processing thin, pinhole-free layers of VO_x on top of the perovskite in n-i-p devices. Cheng et al. recently reported solution-deposited VO_x in the n-i-p architecture; however, they found that the VO_x alone does not conformally coat the underlying perovskite, requiring a >50 nm thick, low band gap (1.5eV) nickel(II) phthalocyanine-based interlayer to improve coverage.[37] Vapor-based synthesis techniques, such as evaporation, sputtering, chemical vapor deposition and ALD, offer viable alternatives for depositing thin films of VO_x in n-i-p PSCs. ALD, which consists of alternating self-limiting surface reactions, is particularly intriguing due to the high degree of control it affords over film thickness and composition. Additionally, the saturating and isotropic nature of ALD growth results in dense, conformal film formation over large area substrates.[38]

ALD processing on top of lead halide perovskite materials imposes some experimental constraints that limit the number of practical precursor chemistries. For example, the use of highly-reactive ozone as a co-reagent or plasma-enhanced ALD processes can result in undesirable changes to the perovskite surface chemistry.[39] Therefore, a more benign thermal ALD process with H_2O as the co-reagent is preferred. The low thermal stability of lead halide perovskite films also defines an upper bound on the processing temperature window. Of the various commercially available vanadium precursors, vanadium(V) oxytriisopropoxide (VTIP)[40–44], tetrakis(ethylmethylamino) vanadium(IV) (TEMAV),[45,46] and tetrakis(dimethylamino) vanadium(IV) (TDMAV)[47] all exhibit appreciable per cycle growth rates at low temperatures (≤

150 °C) with H_2O as a co-reagent. For this study, we chose to use VTIP as the metal-organic precursor because it is a liquid with an appreciable vapor pressure at low temperatures (0.29 torr, 45 °C)[43] and because the vanadium is in the 5+ oxidation state facilitating the formation of V_2O_5 over the thermochromic VO_2.

Solution-processed and heavily doped 2,2’,7,7’-tetrakis(N,N-di-p-methoxyphenyl-amine)9,9’-spirobifluorene (Spiro-OMeTAD) remains the most common HTL in n-i-p PSCs; it also accounts for the largest amount of photocurrent loss in n-i-p PSC/c-Si 2-terminal tandems - up to 2.7 mA/cm^2 for a 100 nm thick layer.[15] Spiro-OMeTAD parasitically absorbs not only in the UV and visible regions of the spectrum, but in the near infrared (NIR) as well, due to polaronic absorption caused by doping to increase its conductivity.[17,48,49] These dopants are also a potential source of instability[50]. To reduce parasitic absorption in the HTL, two strategies can be taken: reduce the thickness of the HTL (to shorten the path length of light through the layer) or reduce the doping in the HTL (to decrease the amount of polaronic absorption). Spin-coating thin layers (<100 nm) of spiro-OMeTAD results in pinholes that negatively impact the open-circuit voltage of devices.[48] Employing an alternative HTL, such as thermally evaporated, un-doped 2,2’,7,7’-tetrakis-(N,N,-di-p-methylphenylamino)-9,9’-spirobifluorene (spiro-TTB), permits a reduction in absorption via both strategies. Spiro-TTB is an organic small molecule that has previously been used as a replacement for spiro-OMeTAD in PSCs and as an HTL in textured PSC/c-Si tandems.[12,51] Both organic species are spiro-linked molecules with mobilities in the range of 10^{-5} to 10^{-4} cm^2/V·s,[52,53] band gaps around 3 eV and ionization potentials within 100 meV of each other.[51]

In this study, we present an advancement for both sputter buffer layers and HTLs for semi-transparent n-i-p PSCs. With a focus on improved photocurrent generation, we have developed a hole contact bilayer on top of the perovskite consisting of a thermally evaporated 30 nm layer of undoped spiro-TTB followed by a thin 9 nm layer of air-stable VO_x by ALD. This bilayer allows for the subsequent sputtering of a transparent indium tin oxide (ITO) top electrode in the same way that ALD SnO_2 enables the sputtering of a TCO for tandems with p-i-n PSCs. The low absorption of UV and visible light in the spiro-TTB layer results in the fabrication of a semi-transparent PSC with a 2.3 mA/cm^2 or 14% increase in photocurrent relative to a device with spiro-OMeTAD, without a deleterious effect on cell voltage. Our design also leverages the conformal, compact nature of the ALD buffer layer to help slow the thermal degradation of mixed cation, mixed halide perovskite films. We show that VO_x in conjunction with an ITO electrode results in a stable semi-transparent device with thin, metal silver fingers for at least 1000 hours of thermal aging at 85°C in a N_2 environment. This work helps to address two critical issues limiting the performance of n-i-p tandems, specifically parasitic absorption and long-term stability of the hole contacts, and offers a route towards achieving high efficiency tandems that are on par with their p-i-n analogs.

Results and Discussion

The ALD VO_x in this study was deposited using vanadium oxytriisopropoxide (VTIP) as the metal-organic precursor and water as the counter-reactant and source of oxygen. To understand the effect of ALD temperature on the underlying perovskite material, we used X-ray diffraction (XRD) to monitor the bulk crystalline phase of a $Cs_{0.17}FA_{0.83}Pb(Br_{0.17}I_{0.83})_3$ (hereafter denoted 17/17 for the 17% Cs^+ composition and 17% Br^- composition) perovskite layer before and after VO_x deposition (Figure 1a, Figure S2). One indication of perovskite degradation is an increase in lead iodide (PbI_2) signal relative to metal halide perovskite signal;[54] as such, we used the ratio of the integrated area of the (001) PbI_2 peak at a 2θ scattering angle of ~12.6 degrees to that of the (100) metal halide perovskite peak at a 2θ scattering angle of ~14.0 degrees as a metric of degradation. As summarized in Figure 1a, an as-deposited perovskite film shows no initial presence of PbI_2; however, after 250 cycles of ALD processing at 100°C on the bare perovskite film, a significant amount of PbI_2 is detected. Additionally, there is visible discoloration of the perovskite film (Figure S3). The formation of PbI_2 following ALD has previously been observed for the growth of SnO_2 buffer layers on top of perovskite at temperatures above 110°C.[55] In that study, Palmstrom et al. link the degradation to an interaction between the perovskite and metal-organic ALD precursor resulting in the removal of the organic cation. It is possible that a similar reaction is occurring between the perovskite and the isopropoxide ligand of the VTIP precursor. With the addition of an interfacial spiro-OMeTAD (150 nm) or spiro-TTB (30 nm) layer on top of the perovskite, the ratio of the PbI_2 peak area relative to that of the perovskite peak decreases from 0.38 to 0.06 and 0.17, respectively. There is less degradation with the spiro-OMeTAD likely because it is much thicker than the spiro-TTB. If the ALD temperature is dropped to 80°C,

PbI_2 formation is greatly reduced for bare perovskite and completely suppressed with either organic interlayer. For this reason, ALD films in this study were deposited at 80°C unless noted otherwise. At this growth temperature, grazing incidence XRD of the ALD VO_x reveals that the as-deposited films are amorphous (Figure S4).

The spiro-TTB and VO_x layers must also exhibit minimal parasitic absorption and conformally cover the underlying perovskite surface to act as effective hole transport and sputter buffer layers in a semi-transparent PSC. Parasitic absorption was assessed by UV-Vis absorption measurements of the bilayers (Figure 1b). From Figure 1b, it is evident that there is a substantial reduction in parasitic absorption when undoped, evaporated spiro-TTB replaces spin-coated spiro-OMeTAD doped with lithium bis(trifluoromethanesulfonyl)imide (LiTFSI) and 4-tert-butylpyridine (tBP) as the HTL. The reduction in absorption in the UV ($\lambda < 400$ nm) is a result of reduced film thickness of the spiro-TTB as compared to spiro-OMeTAD, since this absorption represents optical band gap absorption for both materials.[51] The reduced absorption at longer wavelengths stems from a lower doping density of the spiro-TTB film, thereby diminishing sub-band gap polaronic states that contribute parasitic absorption features.[49] Additionally, ALD VO_x (9 nm) by itself exhibits negligible absorption at wavelengths longer than 500 nm (Figure S5).

Atomic force microscopy (AFM) images in Figure 1c show that the ALD VO_x film is continuous over the perovskite morphological grains with a small amount of secondary texturing. Surface roughness values were obtained by scanning a larger 5 µm x 5 µm area (shown in Figure S6). The initial 17/17 perovskite film had a symmetric height distribution (Table S1) and root-mean-square roughness (R_q) of 17.8 nm. The smooth perovskite surface was deposited using a solvent mixture of 1:1 DMF:DMSO in the precursor solution, which has been shown previously to reduce surface texture.[56] After deposition of a 30 nm spiro-TTB layer on top of said perovskite, the resulting R_q is 18.3 nm, indicating that the thermally evaporated layer does not significantly change the surface roughness. With the addition of 9 nm of VO_x by ALD, the roughness slightly increases to 19.2 nm, but the surface height distribution remains symmetric (indicated by the negligible absolute skewness value in Table S1), further supporting the formation of a coalesced ALD film on the organic HTL that follows the underlying substrate morphology rather than separate islands.

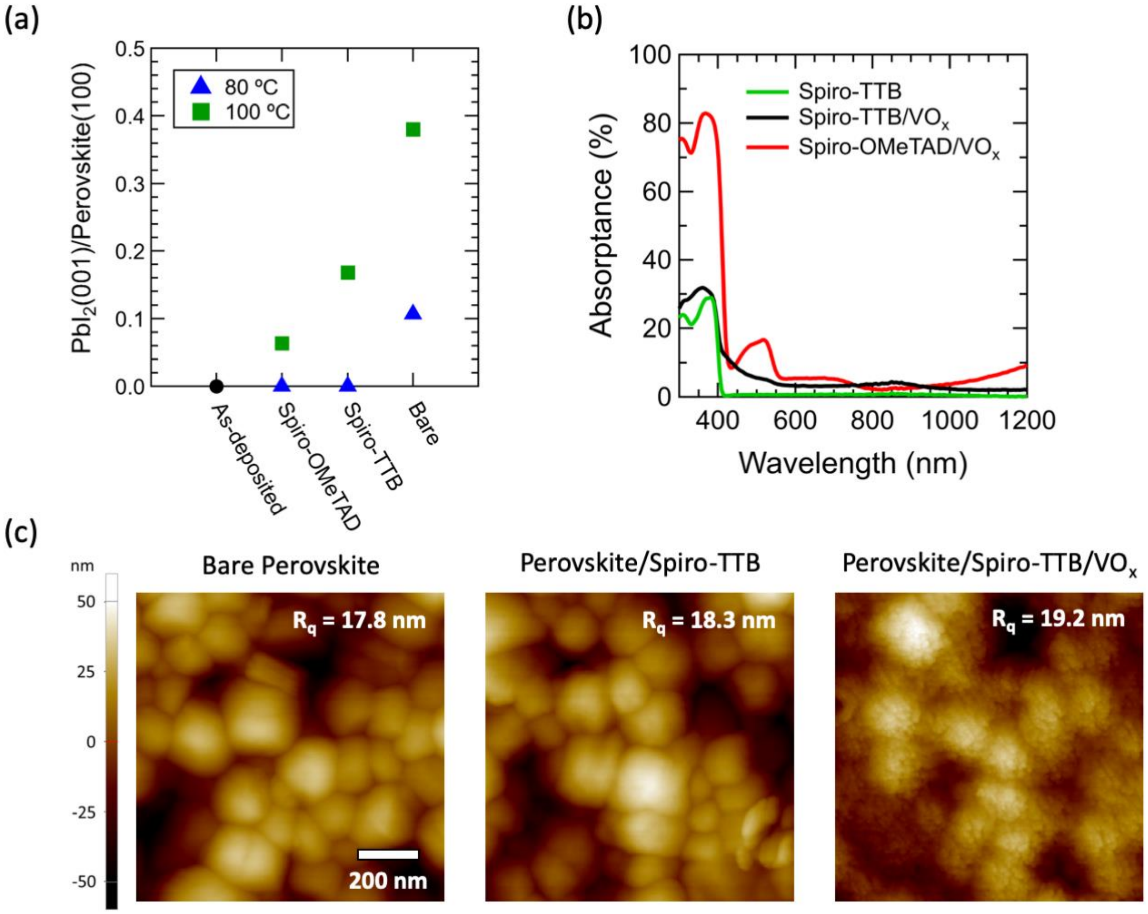

Figure 1: (a) Integrated area ratios of the PbI_2 (001) and perovskite (100) XRD peaks before and after 250 cycles of ALD VO_x processing at 80 °C and 100 °C. Results are presented for a bare perovskite film, as well as those with either a spiro-OMeTAD or spiro-TTB interfacial layer (b) A comparison of the absorption spectra of undoped spiro-TTB (30 nm), spiro-TTB/VO_x (9 nm) and doped spiro-OMeTAD (150 nm)/VO_x on quartz (c) AFM images of spiro-TTB and spiro-TTB/VO_x on a $Cs_{0.17}FA_{0.83}Pb(Br_{0.17}I_{0.83})_3$ perovskite film over a 1 µm x 1 µm scan area. Root mean square roughness (R_q) values are reported in the upper right hand corner of each image

To demonstrate the effectiveness of the spiro-TTB/VO_x bilayer as a hole collector and buffer for subsequent sputtering of a TCO, we fabricated both opaque and semi-transparent single-junction solar cells. The complete device stack chosen for this study and a representative SEM image are shown in Figures 2a,b. We employed a perovskite layer with the aforementioned 17/17 composition and a 1.63 eV band gap for its reported environmental and photo-stability.[14] The electron transport layer (ETL) was a 40 nm layer of spin-coated tin oxide (SnO_2) nanoparticles covered with 15 nm of thermally evaporated C_{60}. The choice of this ETL was supported by previous studies demonstrating improved stability and reduced hysteresis with SnO_2 and C_{60}, respectively.[28,57–60] Finally, in semi-transparent devices, a standard gold electrode was replaced with 150 nm of sputtered ITO with 130 nm thick silver fingers on either side of the active area to facilitate carrier collection.

The thicknesses of the spiro-TTB and VO_x layers were both optimized with respect to device performance. The current-voltage behavior of opaque cells with spiro-TTB thicknesses ranging from 15 nm to 50 nm is presented in Figure S7. From these results, the spiro-TTB layer appears optimized at a thickness of 30 nm. At lower thicknesses, we hypothesize that the spiro-TTB does not sufficiently protect the perovskite from precursor exposure during the first few cycles of ALD. This effect could damage the perovskite material, resulting in less extracted photocurrent observed with 15 nm of spiro-TTB and a lower device yield. At higher thicknesses, an increase in parasitic absorption is expected. A resistivity of 1.7×10^5 Ω-cm was measured for the spiro-TTB layer (Figure S8) and used to estimate series resistance values of 0.5 Ω-cm^2 and 0.9 Ω-cm^2 for 30 nm and 50 nm of spiro-TTB, respectively. This relatively small increase in series resistance is not expected to have a large impact on fill factor and overall device performance. For VO_x thickness optimization, semi-transparent solar cells were made using spiro-OMeTAD and ALD VO_x buffer layers with thicknesses ranging from 6 nm to 18 nm. In general, the device performance increases with thickness and then plateaus (Figure S9). With a 6 nm layer of VO_x, there is sharp s-kink in the current-voltage curve of the solar cell, which is resolved with thicknesses of VO_x above 9 nm. The s-kink at low thicknesses is attributed to damage of the underlying HTL during ITO sputtering, and has been previously observed with MoO_x sputter buffer layers.[21] While thicker buffer layers can offer additional protection from the ITO sputter process, they necessitate longer ALD processing times. Therefore, a VO_x buffer layer thickness of 9 nm was employed for subsequent devices.

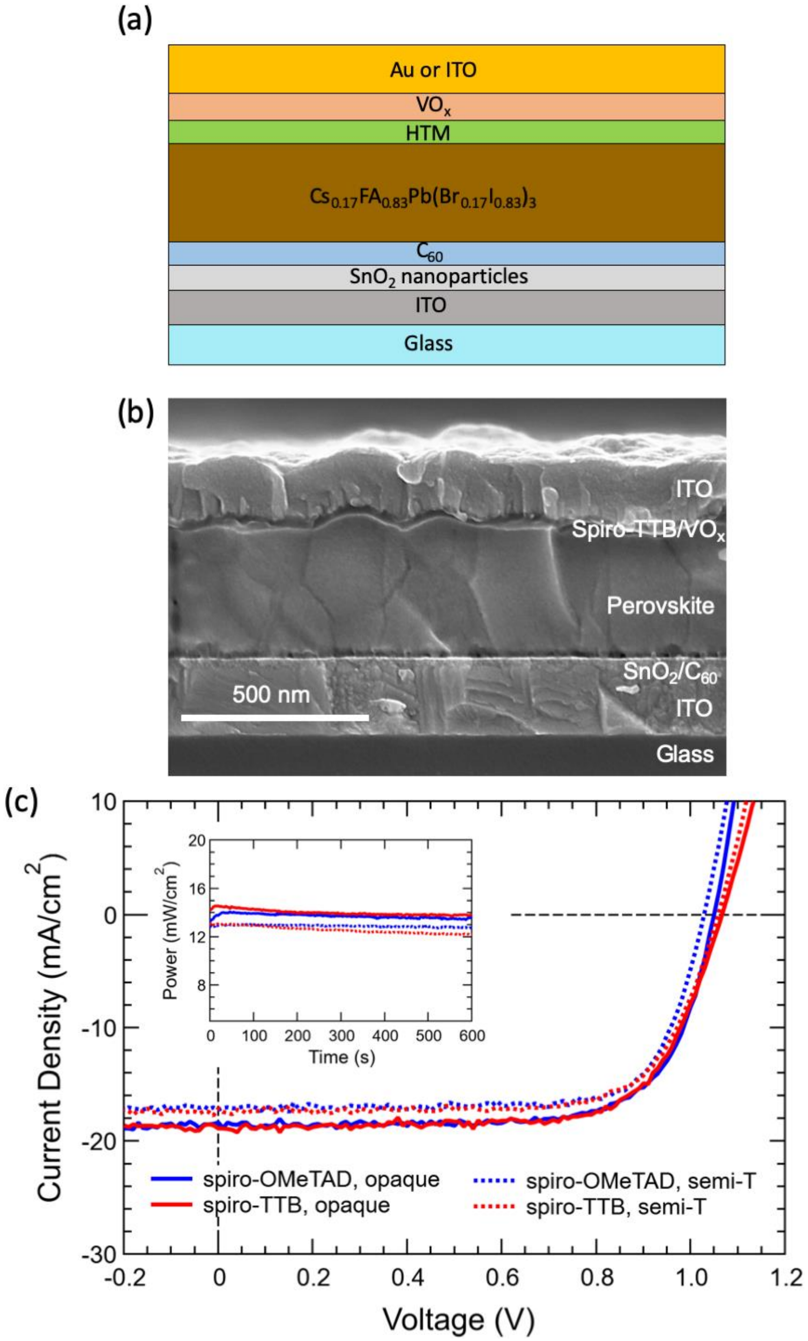

Figure 2: (a) A schematic of an opaque (Au top contact) and semi-transparent (ITO top contact) single-junction perovskite solar cell (b) SEM cross-section image of a semi-transparent single-junction perovskite solar cell (c) Current-voltage (J-V) curves comparing the performance of opaque and semi-transparent single-junction devices illuminated through the glass substrate with spiro-OMeTAD and spiro-TTB as the HTLs. The J-V scans were measured from positive to negative bias. Maximum power-point tracking performance of the same devices for 10 minutes of operation is shown in the inset.

Photovoltaic performance of the best opaque and semi-transparent devices fabricated with the optimal spiro-TTB and VO_x thicknesses, as well as control devices with spiro-OMeTAD/VO_x are presented in Figure 2c and Table S2 with a summary of performance statistics for each device type given in Figure S10 and Table S3. These measurements were taken illuminated through the ETLs and are therefore relatively unaffected by HTL absorption. The power conversion efficiencies of the opaque cells are 14.1% and 14.2% for spiro-OMeTAD and spiro-TTB devices, respectively. The efficiencies of the semi-transparent cells are 13.4% and 13.2% for spiro-OMeTAD and spiro-TTB devices, respectively. In comparing the photovoltaic performances of the devices, there are two main takeaways: (1) spiro-TTB can replace spiro-OMeTAD as an effective HTL in both opaque and semi-transparent cells without a significant reduction in device performance and (2) VO_x is an effective TCO sputter buffer layer, in that replacing the opaque electrode with an ITO electrode does not substantially hurt device efficiency. The small drop in efficiency in the semi-transparent cells stems primarily from reduced photocurrents and is attributed to a reduction in path length of light in the devices, as unabsorbed light is no longer reflected off the opaque contacts back into the device. This effect is also observed when comparing the average performance parameters for each device type in Figure S10. The inset of Figure 2c shows maximum power point tracking (MPPT) of the opaque and semi-transparent devices over 10 minutes of continuous operation. A comparison of the current-voltage characteristic and initial PCE from MPPT (Table S2) for each device implies there is not significant hysteresis behavior for either HTM.

Although the performance of semi-transparent devices fabricated with spiro-TTB and spiro-OMeTAD are similar when illuminated through the ETL side, we are primarily interested in their performance as front-cells in a 2-terminal tandem configuration. Therefore, we additionally measured the photovoltaic behavior and optical properties of devices illuminated through the sputtered ITO and HTL side. To assess the extent to which the difference in absorption shown in Figure 1b translates to increased photocurrent in the perovskite, we measured external quantum efficiency (EQE), transmission, and reflection as a function of wavelength for semi-transparent cells with an optimized, 100 nm anti-reflective layer of MgF_2 on the front surface (see Figure S11 for simulation results of the optimal MgF_2 thickness) These results, as well as the current-voltage behavior of the devices when illuminated though the HTL, are presented in Figure 3. Table S4 lists a summary of the solar cell parameters.

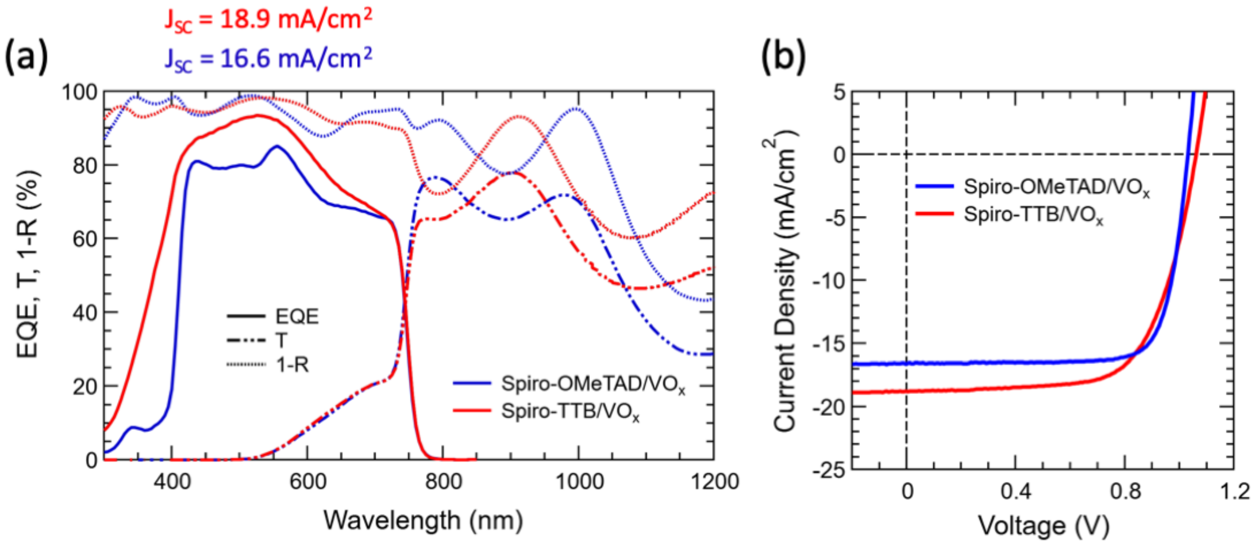

Figure 3: (a) EQE, transmittance, and 1-reflectance of semi-transparent 17/17 perovskite solar cells with spiro-OMeTAD/VO$_x$ and spiro-TTB/VO$_x$ HTLs when illuminated through the top ITO electrode. Integrated J$_{SC}$ values obtained from the EQE spectra are listed above the plot (b) Corresponding current-voltage performance of the same perovskite solar cells when illuminated through the top ITO electrode.

The advantage of using spiro-TTB as an HTL in place of spiro-OMeTAD is evident from a comparison of the two EQE traces. The lower absorption in the spiro-TTB/VO$_x$ bilayer can be seen in the substantial improvement in EQE in the ultraviolet and visible regions as compared to the cell with spiro-OMeTAD/VO$_x$. This increase in EQE corresponds to a 2.3 mA/cm^2 (from 16.6 mA/cm^2 to 18.9 mA/cm^2) or a 14% boost in photocurrent under one sun of AM1.5 solar irradiance. Strong optical interference within the thin-film semi-transparent stack produces the large features observed in the measured reflection spectra for wavelengths above 800 nm. We used one-dimensional transfer matrix modeling (TMM) to help predict the optical behavior of the semi-transparent PSC when it is monolithically stacked on top of a heterojunction silicon cell with an ITO recombination layer.[61] The simulation of a 2-terminal tandem that incorporates the optimized perovskite front cell shown in Figure 2a with a 160 nm ITO recombination layer and a thinner, 40 nm top ITO contact to minimize the reflections observed in Figure 3a, estimates a photocurrent of 17.8 mA/cm^2 in a bottom heterojunction silicon cell (Figures S12, S13). This photocurrent in the silicon sub-cell is slightly higher than that of the best reported PSC/c-Si 2-terminal tandem in the n-i-p architecture, while maintaining 18.5 mA/cm^2 of photocurrent in the PSC and without thinning the 415 nm perovskite layer to increase the transmission of light to the bottom cell.[15] These thicknesses for the recombination layer and top contact are predicted to maximize current in the silicon cell, while also maintaining a high photocurrent in the perovskite cell (Figure S14). Previous works have successfully demonstrated the use of thin TCO front contacts with metal gridlines on top to help with lateral current collection; 40 nm of indium zinc oxide (IZO) and 60 nm of ITO were used as front contacts in the fabrication of 22.5% n-i-p and 25% p-i-n monolithic PSC/c-Si tandem cells, respectively.[15,23] Further optimization of the perovskite thickness and band gap, improving transparency of the interconnecting layers, or fabrication of the PSC on a textured silicon cell to improve light trapping could be used to further equal the distribution of the 2.3 mA/cm^2 of additional photocurrent afforded by the spiro-TTB/VO_x bilayer between the two sub-cells, boosting the achievable matched photocurrent of a tandem cell beyond 17.8 mA/cm^2.

Given that a hypothesized advantage to replacing MoO_x with VO_x is improved stability, both the chemical and thermal stability of films and devices made with the VO_x sputter buffer layer were investigated. To probe the chemical stability of the ALD VO_x film by itself, as well as with the underlying perovskite, X-ray photoelectron spectroscopy (XPS) was implemented to monitor the oxidation state of vanadium atoms. Previous researchers have used oxidation state as a metric for monitoring chemical interactions at the interfaces of MoO_x films in perovskite devices; for example, Schulz et al. have shown that the reduction of a Mo^{6+}/Mo^{5+} film to Mo^{4+} due to interactions with the perovskite is correlated with a rapid decline in device performance.[25] Similar measurements were taken on VO_x films grown by ALD at 80°C on silicon substrates immediately following deposition and after one week of ambient air exposure. Additionally, the oxidation states of ALD VO_x films grown directly on 17/17 perovskite and on perovskite capped with a spiro-TTB HTL were measured. In all cases, a thinner ~4 nm layer of VO_x (100 ALD cycles) was grown and XPS peaks unique to the substrate were detected (Si2p for silicon, Pb4d, Cs3d, I3d for perovskite and C1s, N1s for spiro-TTB; XPS survey spectra are shown in Figure S15), indicating that the data reflect the entire VO_x film including the interfaces. These results are presented in Figure 4a.

The XPS spectra in Figure 4a highlight vanadium 2p and oxygen 1s core levels. Due to the proximity of their binding energies (BE), the peaks were fit together after subtracting out a Shirley background, analogous to previous XPS studies of vanadium oxide.[62] We estimated the relative percentages of the various oxidation states of vanadium oxide by fitting the emitted photoelectron peaks and calculating the areas under the curves. Based on the oxidation state of vanadium in the VTIP precursor, a stoichiometric ALD VO_x film would have 100% of the vanadium in the 5+ oxidation state; however, partial reduction of the vanadium oxide film during deposition and after air exposure is frequently observed.[63–65] Using the integrated areas of the V^{4+} and V^{5+} fitted peaks from either the $V2p_{3/2}$ (BEs of 515.8ev and 517.0eV, respectively) or $V2p_{1/2}$ (BEs of 523.1 and 524.3, respectively) component, it was observed that 17% of the vanadium in the as-deposited film was in the V^{4+} state and the remainder was in the V^{5+} state. After one week of ambient air exposure, 14% of the vanadium was in the V^{4+} state, indicating that the neat film did not undergo a significant chemical change upon air exposure and that maintaining an inert environment before deposition of the TCO top contact is not required. When ALD VO_x is deposited directly on perovskite, an increase in the V^{4+} species to 40% was observed, suggesting that the metal oxide reacts to some extent when in direct contact with the perovskite. However, unlike MoO_x which has been shown to reduce from Mo^{6+}/Mo^{5+} to a Mo^{4+} state not initially present in the film, we detected no further reduced vanadium species (e.g. V^{3+}, V^{2+} etc.). When a thin, 30 nm layer of spiro-TTB was deposited between the VO_x and perovskite, we observed a drop in the relative amount of V^{4+} to 28%. In this scenario, the VO_x is likely preferentially oxidizing the spiro-TTB, resulting in an increase in reduced vanadium species relative to the as-deposited film. This exchange could lead to charge-transfer doping at the interface and the appearance of the broad absorption feature at 850 nm in the UV-Vis spectrum of the spiro-TTB/VO_x bilayer in Figure 1b, similar to the remote doping of HTLs by MoO_x observed by Xu et al.[66] Reduction of the vanadium might also be causing sub-band gap absorption in the oxide, akin to the coloration of WO_3 films following metal reduction.[67]

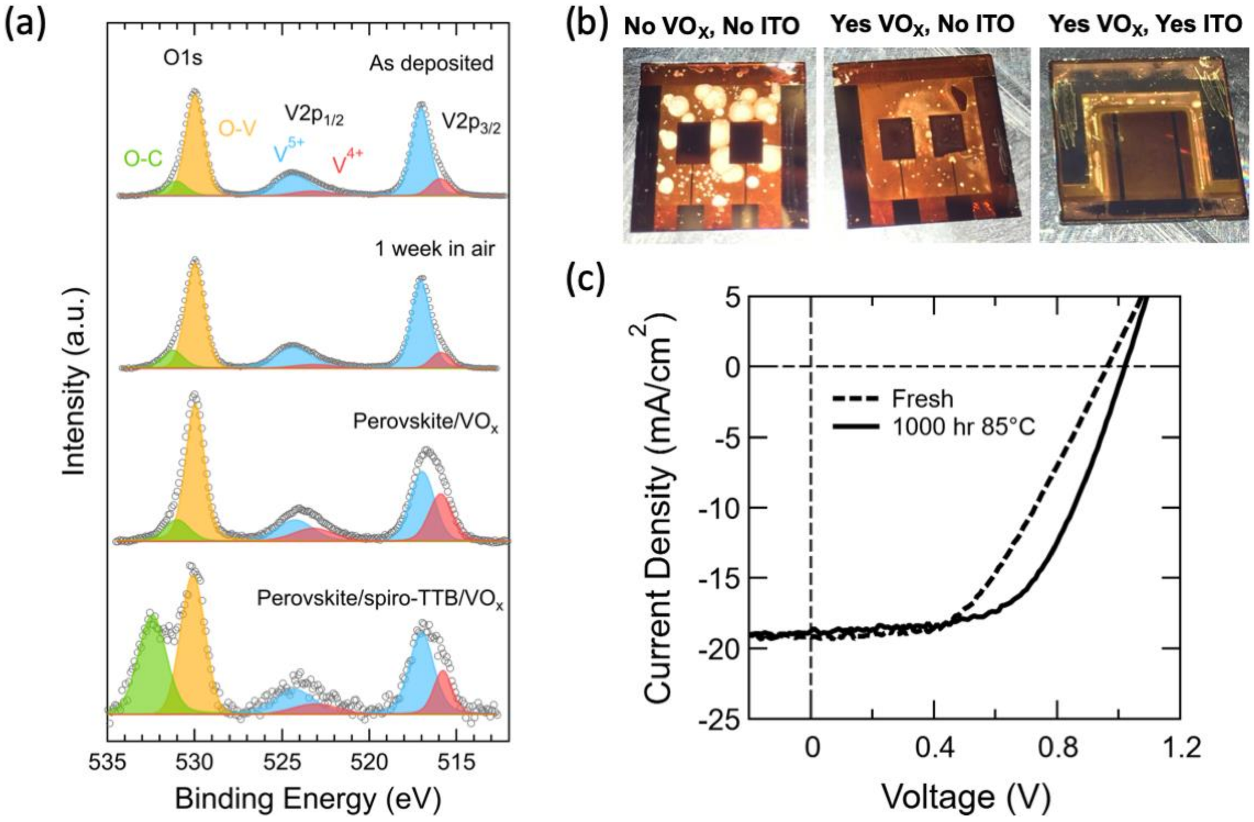

Figure 4: (a) XPS spectra of the V2p doublet and O1s peak of an ALD VO_x film as-deposited and after 1 week of ambient air exposure, as well as deposited on a 17/17 perovskite film with and without an interfacial spiro-TTB layer (b) Photographs of 17/17 perovskite solar cells with and without a VO_x/ITO top contact after 1000 hours of thermal aging at 85°C in an inert N_2 environment (c) Current-voltage curves for the device with a VO_x/ITO top contact before and after 1000 hours of thermal aging at 85°C in an inert N_2 environment.

The ambient exposure results suggest that the reduced reactivity of the VO_x makes it compatible with long-term device stability. To test stability, devices with three types of contacts were fabricated and thermally aged for 1000 hours at 85°C in an inert N_2 environment: (1) a 100 nm gold contact only (2) 9 nm VO_x and a 100 nm gold contact and (3) 9 nm VO_x and a 150 nm sputtered ITO contact. All three devices used spiro-OMeTAD as the HTL, and no additional encapsulation layers were added for the stability testing. Top view photographs of the devices after thermal aging are shown in Figure 4b. It is apparent from the images that the perovskite cell with neither VO_x nor ITO experienced substantial visible degradation over 1000 hours. During the aging process, a significant portion of the visible perovskite area had been optically bleached from the normal dark-brown perovskite color to a pale-yellow indicative of PbI_2 and the device was no longer functional. This result is consistent with previous reports that spiro-OMeTAD is not an appropriate contact material for long term stability; it is easily permeable to volatile degradation products leaving the perovskite and metal diffusion down into the device.[68,69] Adding the VO_x buffer layer appeared to substantially slow the degradation process, with a large reduction in bleached area. Finally, with a sputtered ITO electrode (area between the silver metal fingers in right-most photograph), there was no visible degradation after 1000 hours of thermal aging, and the current-voltage performance of the device slightly improved (Figure 4c), potentially from improved crystallinity and grain ripening in the perovskite film. This preliminary thermal stability study is promising and suggests that: (1) VO_x/ITO is an effective diffusion barrier and (2) the presence of VO_x does not lead to a reduction in device performance following prolonged thermal stress. Further testing is required to probe the long-term thermal stability of devices with undoped spiro-TTB; however, given the similarity of the spiro-TTB and spiro-OMeTAD molecules, we expect similar results for cells with spiro-TTB that employ the ALD VO_x/ITO electrode.

Conclusions

The use of PSCs in tandem devices offers an exciting pathway towards high-efficiency and low-cost photovoltaics; however, 2-terminal PSC/c-Si devices in the n-i-p architecture have yet to live up to their potential. In this work we have developed improved hole contact materials to directly address the optical losses and stability challenges currently limiting the performance of these devices. We have developed a thin, conformal ALD VO_x buffer that is air-stable and protects the underlying perovskite during sputtering of a front TCO contact. Additionally, we show that the low-temperature 80°C ALD process is compatible with $Cs_{0.17}FA_{0.83}Pb(Br_{0.17}I_{0.83})_3$ perovskite. When incorporated into semi-transparent PSCs with a transparent ITO contact, these ALD films show promise as barrier layers for improved long-term thermal stability of PSCs. Furthermore, replacing solution-processed, doped spiro-OMeTAD with thin, undoped spiro-TTB as a hole transport material increases photocurrent in the perovskite front cell by 2.3 mA/cm^2 or 14%. Because both VO_x and spiro-TTB are deposited using vapor methods, this bilayer is also compatible with the fabrication of PSCs on a textured silicon substrate which has been shown to be an effective method for improved current-matching in the two sub-cells and reduced reflection in the NIR. Moving forward, more research of ALD growth behavior on various transport materials should help inform the development of new ALD processes and chemistries that produce better barrier layers and are more compatible with lead halide perovskites. Ultimately, the improvements made in this study encourage further optimization of n-i-p tandems in the quest for PSC/c-Si tandem efficiencies beyond 30%.

Conflicts of Interest

There are no conflicts to declare.

Acknowledgements

The information, data, and work presented were funded by the U.S. Department of Energy (DOE) PVRD2 program under Award No. DE-EE0008154. R.A.B was supported by the National Science Foundation EAGER under award number 1664669. R.P. was supported by the Office of Naval Research under award number N00014-17-1-2212. Part of this work was performed at the Stanford Nano Shared Facilities (SNSF) and the Stanford Nanofabrication Facility (SNF), supported by the National Science Foundation under award ECCS-1542152. The authors would like to thank Camila De Paula for SEM imaging, Wen Ma and Farhad Moghadam of Sunpreme, Sunnyvale, CA for ITO sputtering, and Tomas Leijtens and Caleb Boyd for fruitful discussions.

References

1 C. Battaglia, A. Cuevas and S. De Wolf, *Energy Environ. Sci.*, 2016, **9**, 1552–1576.

2 A. Kojima, K. Teshima, Y. Shirai and T. Miyasaka, *J. Am. Chem. Soc.*, 2009, **131**, 6050–6051.

3 M. M. Lee, J. Teuscher, T. Miyasaka, T. N. Murakami and H. J. Snaith, *Science*, 2012, **338**, 643–647.

4 N. J. Jeon, J. H. Noh, Y. C. Kim, W. S. Yang, S. Ryu and S. Il Seok, *Nat. Mater.*, 2014, **13**, 897–903.

5 M. Saliba, T. Matsui, K. Domanski, J.-Y. Seo, A. Ummadisingu, S. M. Zakeeruddin, J.-P. Correa-Baena, W. R. Tress, A. Abate, A. Hagfeldt and M. Grätzel, *Science*, 2016, **354**, 206–209.

6 National Renewable Energy Laboratory. Best Research-Cell Efficiencies, https://www.nrel.gov/pv/assets/pdfs/pv-efficiencies-07-17-2018.pdf, (accessed 24 January 2019).

7 R. Prasanna, A. Gold-Parker, T. Leijtens, B. Conings, A. Babayigit, H.-G. Boyen, M. F. Toney and M. D. McGehee, *J. Am. Chem. Soc.*, 2017, **139**, 11117–11124.

8 G. E. Eperon, S. D. Stranks, C. Menelaou, M. B. Johnston, L. M. Herz and H. J. Snaith, *Energy Environ. Sci.*, 2014, **7**, 982–988.

9 S. De Wolf, J. Holovsky, S.-J. Moon, P. Löper, B. Niesen, M. Ledinsky, F.-J. Haug, J.-H. Yum and C. Ballif, *J. Phys. Chem. Lett.*, 2014, **5**, 1035–1039.

10 Z. M. Beiley and M. D. McGehee, *Energy Environ. Sci.*, 2012, **5**, 9173–9179.

11 C. D. Bailie, M. G. Christoforo, J. P. Mailoa, A. R. Bowring, E. L. Unger, W. H. Nguyen, J. Burschka, N. Pellet, J. Z. Lee, M. Grätzel, R. Noufi, T. Buonassisi, A. Salleo and M. D. McGehee, *Energy Environ. Sci.*, 2015, **8**, 956–963.

12 F. Sahli, J. Werner, B. A. Kamino, M. Bräuninger, R. Monnard, B. Paviet-Salomon, L. Barraud, L. Ding, J. J. Diaz Leon, D. Sacchetto, G. Cattaneo, M. Despeisse, M. Boccard, S. Nicolay, Q. Jeangros, B. Niesen and C. Ballif, *Nat. Mater.*, 2018, **17**, 820–826.

13 T. Duong, Y. Wu, H. Shen, J. Peng, X. Fu, D. Jacobs, E.-C. Wang, T. C. Kho, K. C. Fong, M. Stocks, E. Franklin, A. Blakers, N. Zin, K. McIntosh, W. Li, Y.-B. Cheng, T. P. White, K. Weber and K. Catchpole, *Adv. Energy Mater.*, 2017, **7**, 1700228.

14 K. A. Bush, A. F. Palmstrom, Z. J. Yu, M. Boccard, R. Cheacharoen, J. P. Mailoa, D. P. McMeekin, R. L. Z. Hoye, C. D. Bailie, T. Leijtens, I. M. Peters, M. C. Minichetti, N. Rolston, R. Prasanna, S. Sofia, D. Harwood, W. Ma, F. Moghadam, H. J. Snaith, T. Buonassisi, Z. C. Holman, S. F. Bent and M. D. McGehee, *Nat. Energy*, 2017, **2**, 17009.

15 Y. Wu, D. Yan, J. Peng, T. Duong, Y. Wan, S. P. Phang, H. Shen, N. Wu, C. Barugkin, X. Fu, S. Surve, D. Grant, D. Walter, T. P. White, K. R. Catchpole and K. J. Weber, *Energy Environ. Sci.*, 2017, **10**, 2472–2479.

16 B. Chen, Z. Yu, K. Liu, X. Zheng, Y. Liu, J. Shi, D. Spronk, P. N. Rudd, Z. Holman and J. Huang, *Joule*, 2019, **3**, 177–190.

17 J. P. Mailoa, C. D. Bailie, E. C. Johlin, E. T. Hoke, A. J. Akey, W. H. Nguyen, M. D. McGehee and T. Buonassisi, *Appl. Phys. Lett.*, 2015, **106**, 121105.

18 D. T. Grant, K. R. Catchpole, K. J. Weber and T. P. White, *Opt. Express*, 2016, **24**, A1454–A1470.

19 J. Werner, L. Barraud, A. Walter, M. Bräuninger, F. Sahli, D. Sacchetto, N. Tétreault, B. Paviet-Salomon, S.-J. Moon, C. Allebé, M. Despeisse, S. Nicolay, S. De Wolf, B. Niesen

and C. Ballif, *ACS Energy Lett.*, 2016, **1**, 474–480.

20 C. C. Boyd, R. Cheacharoen, K. A. Bush, R. Prasanna, T. Leijtens and M. D. McGehee, *ACS Energy Lett.*, 2018, **3**, 1772–1778.

21 J. Werner, G. Dubuis, A. Walter, P. Löper, S.-J. Moon, S. Nicolay, M. Morales-Masis, S. De Wolf, B. Niesen and C. Ballif, *Sol. Energy Mater. Sol. Cells*, 2015, **141**, 407–413.

22 L. S. Liao, L. S. Hung, W. C. Chan, X. M. Ding, T. K. Sham, I. Bello, C. S. Lee and S. T. Lee, *Appl. Phys. Lett.*, 1999, **75**, 1619.

23 K. A. Bush, S. Manzoor, K. Frohna, Z. J. Yu, J. A. Raiford, A. F. Palmstrom, H.-P. Wang, R. Prasanna, S. F. Bent, Z. C. Holman and M. D. McGehee, *ACS Energy Lett.*, 2018, **3**, 2173–2180.

24 J. Werner, C. H. Weng, A. Walter, L. Fesquet, J. P. Seif, S. De Wolf, B. Niesen and C. Ballif, *J. Phys. Chem. Lett.*, 2016, **7**, 161–166.

25 P. Schulz, J. O. Tiepelt, J. A. Christians, I. Levine, E. Edri, E. M. Sanehira, G. Hodes, D. Cahen and A. Kahn, *ACS Appl. Mater. Interfaces*, 2016, **8**, 31491–31499.

26 P. Liu, X. Liu, L. Lyu, H. Xie, H. Zhang, D. Niu, H. Huang, C. Bi, Z. Xiao, J. Huang and Y. Gao, *Appl. Phys. Lett.*, 2015, **106**, 193903.

27 E. M. Sanehira, B. J. Tremolet de Villers, P. Schulz, M. O. Reese, S. Ferrere, K. Zhu, L. Y. Lin, J. J. Berry and J. M. Luther, *ACS Energy Lett.*, 2016, **1**, 38–45.

28 J. A. Christians, P. Schulz, J. S. Tinkham, T. H. Schloemer, S. P. Harvey, B. J. Tremolet de Villers, A. Sellinger, J. J. Berry and J. M. Luther, *Nat. Energy*, 2018, **3**, 68–74.

29 S. Beke, *Thin Solid Films*, 2011, **519**, 1761–1771.

30 M. T. Greiner and Z.-H. Lu, *NPG Asia Mater.*, 2013, **5**, e55.

31 X. Yao, J. Qi, W. Xu, X. Jiang, X. Gong and Y. Cao, *ACS Omega*, 2018, **3**, 1117–1125.

32 X. Yao, W. Xu, X. Huang, J. Qi, Q. Yin, X. Jiang, F. Huang, X. Gong and Y. Cao, *Org. Electron.*, 2017, **47**, 85–93.

33 Z. Liu, T. He, H. Wang, X. Song, H. Liu, J. Yang, K. Liu and H. Ma, *RSC Adv.*, 2017, **7**, 18456–18465.

34 C.-C. Chang, J.-H. Tao, C.-E. Tsai, Y.-J. Cheng and C.-S. Hsu, *ACS Appl. Mater. Interfaces*, 2018, **10**, 21466–21471.

35 T. Lei, H. Dong, J. Xi, Y. Niu, J. Xu, F. Yuan, B. Jiao, W. Zhang, X. Hou and Z. Wu, *Chem. Commun.*, 2018, **54**, 6177–6180.

36 D. Wang, N. K. Elumalai, M. A. Mahmud, M. Wright, M. B. Upama, K. H. Chan, C. Xu, F. Haque, G. Conibeer and A. Uddin, *Org. Electron.*, 2018, **53**, 66–73.

37 M. Cheng, Y. Li, M. Safdari, C. Chen, P. Liu, L. Kloo and L. Sun, *Adv. Energy Mater.*, 2017, **7**, 1602556.

38 R. W. Johnson, A. Hultqvist and S. F. Bent, *Mater. Today*, 2014, **17**, 236–246.

39 V. Zardetto, B. L. Williams, A. Perrotta, F. Di Giacomo, M. A. Verheijen, R. Andriessen, W. M. M. Kessels and M. Creatore, *Sustain. Energy Fuels*, 2017, **1**, 30–55.

40 T. Singh, S. Wang, N. Aslam, H. Zhang, S. Hoffmann-Eifert and S. Mathur, *Chem. Vap. Depos.*, 2014, **20**, 291–297.

41 X. Sun, C. Zhou, M. Xie, T. Hu, H. Sun, G. Xin, G. Wang, S. M. George and J. Lian, *Chem. Commun.*, 2014, **50**, 10703–10706.

42 J. C. Badot, A. Mantoux, N. Baffier, O. Dubrunfaut and D. Lincot, *J. Mater. Chem.*, 2004, **14**, 3411–3415.

43 J. C. Badot, S. Ribes, E. B. Yousfi, V. Vivier, J. P. Pereira-Ramos, N. Baffier and D. Lincotb, *Electrochem. Solid-State Lett.*, 1999, **3**, 485–488.

44 J. Musschoot, D. Deduytsche, H. Poelman, J. Haemers, R. L. Van Meirhaeghe, S. Van den Berghe and C. Detavernier, *J. Electrochem. Soc.*, 2009, **156**, 122–126.

45 T. Blanquart, J. Niinistö, M. Gavagnin, V. Longo, M. Heikkilä, E. Puukilainen, V. R. Pallem, C. Dussarrat, M. Ritala and M. Leskelä, *RSC Adv.*, 2013, **3**, 1179–1185.

46 K. Zhang, M. Tangirala, D. Nminibapiel, W. Cao, V. Pallem, C. Dussarrat and H. Baumgart, *ECS Trans.*, 2013, **50**, 175–182.

47 X. Wang, Z. Guo, Y. Gao and J. Wang, *J. Mater. Res.*, 2017, **32**, 37–44.

48 N. Marinova, W. Tress, R. Humphry-Baker, M. I. Dar, V. Bojinov, S. M. Zakeeruddin, M. K. Nazeeruddin and M. Grätzel, *ACS Nano*, 2015, **9**, 4200–4209.

49 W. H. Nguyen, C. D. Bailie, E. L. Unger and M. D. McGehee, *J. Am. Chem. Soc.*, 2014, **136**, 10996–11001.

50 T. Leijtens, T. Giovenzana, S. N. Habisreutinger, J. S. Tinkham, N. K. Noel, B. A. Kamino, G. Sadoughi, A. Sellinger and H. J. Snaith, *ACS Appl. Mater. Interfaces*, 2016, **8**, 5981–5989.

51 R. A. Belisle, P. Jain, R. Prasanna, T. Leijtens and M. D. McGehee, *ACS Energy Lett.*, 2016, **1**, 556–560.

52 T. Leijtens, J. Lim, J. Teuscher, T. Park and H. J. Snaith, *Adv. Mater.*, 2013, **25**, 3227–3233.

53 T. P. I. Saragi, T. Fuhrmann-Lieker and J. Salbeck, *Adv. Funct. Mater.*, 2006, **16**, 966–974.

54 I. Deretzis, A. Alberti, G. Pellegrino, E. Smecca, F. Giannazzo, N. Sakai, T. Miyasaka and A. La Magna, *Appl. Phys. Lett.*, 2015, **106**, 131904.

55 A. F. Palmstrom, J. A. Raiford, R. Prasanna, K. A. Bush, M. Sponseller, R. Cheacharoen, M. C. Minichetti, D. S. Bergsman, T. Leijtens, H.-P. Wang, V. Bulović, M. D. McGehee and S. F. Bent, *Adv. Energy Mater.*, 2018, **8**, 1800591.

56 K. A. Bush, N. Rolston, A. Gold-Parker, S. Manzoor, J. Hausele, Z. J. Yu, J. A. Raiford, R. Cheacharoen, Z. C. Holman, M. F. Toney, R. H. Dauskardt and M. D. McGehee, *ACS Energy Lett.*, 2018, **3**, 1225–1232.

57 T. Leijtens, G. E. Eperon, S. Pathak, A. Abate, M. M. Lee and H. J. Snaith, *Nat. Commun.*, 2013, **4**, 2885.

58 B. Roose, J.-P. C. Baena, K. C. Gödel, M. Grätzel, A. Hagfeldt, U. Steiner and A. Abate, *Nano Energy*, 2016, **30**, 517–522.

59 K. Wojciechowski, T. Leijtens, S. Siprova, C. Schlueter, M. T. Hörantner, J. T.-W. Wang, C.-Z. Li, A. K.-Y. Jen, T.-L. Lee and H. J. Snaith, *J. Phys. Chem. Lett.*, 2015, **6**, 2399–2405.

60 H. Yoon, S. M. Kang, J.-K. Lee and M. Choi, *Energy Environ. Sci.*, 2016, **9**, 2262–2266.

61 G. F. Burkhard, E. T. Hoke and M. D. McGehee, *Adv. Mater.*, 2010, **22**, 3293–3297.

62 G. Silversmit, D. Depla, H. Poelman, G. B. Marin and R. De Gryse, *J. Electron Spectros. Relat. Phenomena*, 2004, **135**, 167–175.

63 K. Zilberberg, S. Trost, J. Meyer, A. Kahn, A. Behrendt, D. Lützenkirchen-Hecht, R. Frahm and T. Riedl, *Adv. Funct. Mater.*, 2011, **21**, 4776–4783.

64 T. Blanquart, J. Niinistö, M. Gavagnin, V. Longo, M. Heikkilä, E. Puukilainen, V. R. Pallem, C. Dussarrat, M. Ritala and M. Leskelä, *RSC Adv.*, 2013, **3**, 1179–1185.

65 J. Meyer, K. Zilberberg, T. Riedl and A. Kahn, *J. Appl. Phys.*, 2011, **110**, 033710.

66 J. Xu, O. Voznyy, R. Comin, X. Gong, G. Walters, M. Liu, P. Kanjanaboos, X. Lan and E. H. Sargent, *Adv. Mater.*, 2016, **28**, 2807–2815.

67 G. Leftheriotis, S. Papaefthimiou, P. Yianoulis and A. Siokou, *Thin Solid Films*, 2001, **384**, 298–306.
68 K. Domanski, J.-P. Correa-Baena, N. Mine, M. K. Nazeeruddin, A. Abate, M. Saliba, W. Tress, A. Hagfeldt and M. Grätzel, *ACS Nano*, 2016, **10**, 6306–6314.
69 Y. Kato, L. K. Ono, M. V. Lee, S. Wang, S. R. Raga and Y. Qi, *Adv. Mater. Interfaces*, 2015, **2**, 1500195.